Doubled Thermoelectric Figure of Merit in p-Type β-FeSi$_2$ via Synergistically Optimizing Electrical and Thermal Transports

Xiaolong Du, Pengfei Qiu,* Jun Chai, Tao Mao, Ping Hu, Jiong Yang, Yi-Yang Sun, Xun Shi,* and Lidong Chen

Read Online

ACCESS | Metrics & More | Article Recommendations | Supporting Information

ABSTRACT: β-FeSi$_2$ has long been investigated as a promising thermoelectric (TE) material working at high temperatures due to its combining features of environmental friendliness, good thermal stability, and strong oxidation resistance. However, the real application of β-FeSi$_2$ is still limited by its low TE figure of merit (zT). In this study, nearly doubled zT in p-type β-FeSi$_2$ has been achieved via synergistically optimizing electrical and thermal transports. Based on the first-principles calculations, Al with shallow acceptor transition level and high carrier donation efficiency is chosen to dope β-FeSi$_2$. Significantly improved electrical transport, particularly in the low temperature range, has been obtained in the Al-doped β-FeSi$_2$ system. The power factor for FeSi$_{1.96}$Al$_{0.04}$ at 300 K is even higher than that of p-type β-FeSi$_2$-based compounds reported previously at high temperatures. By alloying β-FeSi$_2$ with Os at the Fe sites, we further lower the lattice thermal conductivity. Fe$_{0.80}$Os$_{0.20}$Si$_{1.96}$Al$_{0.04}$ possesses the lowest lattice thermal conductivity among the β-FeSi$_2$ compounds prepared by the equilibrium method. Finally, a record-high zT value of 0.35 is obtained for p-type Fe$_{0.80}$Os$_{0.20}$Si$_{1.96}$Al$_{0.04}$. This study is expected to accelerate the application of β-FeSi$_2$.

KEYWORDS: *thermoelectric, β-FeSi$_2$, electrical transport, lattice thermal conductivity, transition level*
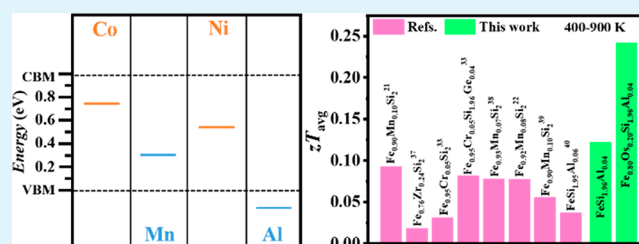
1. INTRODUCTION

The decline of fossil energy promotes the great interest in developing waste heat recovery techniques. Thermoelectric (TE) technology can recover the waste heat discharged by the automobiles and manufacturing industry, providing an alternative way to more efficiently utilize fossil energy.[1−4] The ability of TE technology to convert the waste heat into useful electricity is dependent on the material's dimensionless TE figure of merit, $zT = S^2\sigma T/\kappa$, where S, σ, T, and κ are the Seebeck coefficient, electrical conductivity, absolute temperature, and thermal conductivity, respectively. The PF ($= S^2\sigma$) determines the performance of electrical transports. The κ consists of the lattice thermal conductivity κ_L and carrier thermal conductivity κ_e. High zT requires high σ, large S, and low κ_L.[5] Doping and alloying are the common strategies to tune σ, S, and κ_L. Beyond the type and concentration of the dopants, the carrier donation efficiency is also an important factor because it directly determines the ability of dopants to influence the electrical transports. However, it is rarely considered in thermoelectrics.

Among the various kinds of TE materials, β-FeSi$_2$ has for long been investigated as a promising TE material working at high temperatures.[6−10] β-FeSi$_2$ crystallizes in orthogonal structure with the space group of *Cmca*.[11] Its optical band gap is around 0.8 eV.[12] Compared to other TE materials, the advantages of β-FeSi$_2$ lie in its environmental friendliness, good

thermal stability, and strong oxidation resistance.[13,14] β-FeSi$_2$ can work in atmospheric conditions for a wide temperature range from 300 to 1173 K without any extra coating, which greatly facilitates the fabrication of the TE device working at high temperatures.[15,16] However, so far, the real application of β-FeSi$_2$ is still limited because of its low zT. Although many elements (e.g., Co,[17−20] Mn,[21−23] and Ni[24,25]) in the periodic table have been doped into β-FeSi$_2$, its zT is still much lower than the state-of-the-art TE materials. The maximum zT value for n-type β-FeSi$_2$ is 0.33 at 900 K.[20] The value is even lower for p-type β-FeSi$_2$, about 0.21 at 1040 K.[21] Thus, improving the zT of β-FeSi$_2$ is still the most important task for its real applications.

The low zT of β-FeSi$_2$ mainly comes from two aspects, termed the low σ and high κ_L. Generally, the σ values of the state-of-the-art TE materials are on the order of 10^4-10^5 S m^{-1}.[4,26−30] However, most of the doped β-FeSi$_2$ compounds reported so far have the σ values only on the order of $10-10^3$ S m^{-1} at 300 K. Until the temperature is raised to as high as
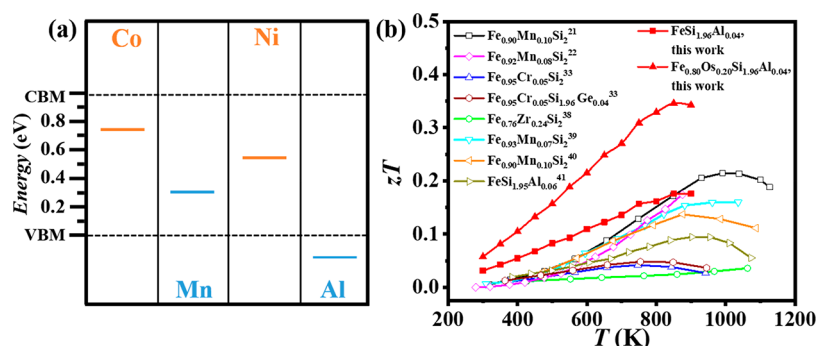
Figure 1. (a) Defect transition level of Al in β-FeSi$_2$ calculated by using the SCAN functional based on a 96-atom supercell. The data of Co, Ni, and Mn taken from ref 31 are included for comparison. The donor and acceptor levels are marked by brown and blue color, respectively. (b) TE figure of merit (zT) for FeSi$_{1.96}$Al$_{0.04}$ and Fe$_{0.80}$Os$_{0.20}$Si$_{1.96}$Al$_{0.04}$ in this work. The data of some p-type β-FeSi$_2$-based compounds reported previously are also included for comparison.[21,22,33,38−41]

700−800 K, the σ values can be increased to 10^4 S m^{-1}.[21−25] Hence, in spite of the large S, the doped β-FeSi$_2$ compounds usually possess very low PF in the low temperature range, such as 2.2 μW cm^{-1} K^2 for Fe$_{0.90}$Mn$_{0.10}$Si$_2$ at 300 K[21] and 0.17 μW cm^{-1} K^2 for Fe$_{0.94}$Ni$_{0.06}$Si$_2$ at 300 K.[24] These low σ and PF are originated from the low carrier concentrations, such as 1.4 × 10^{19} cm^{-3} for Fe$_{0.90}$Mn$_{0.10}$Si$_2$ and 4.7 × 10^{19} cm^{-3} for Fe$_{0.97}$Ni$_{0.03}$Si$_2$ at 300 K.[21,25] Generally, the ability of a dopant to donate carriers is simultaneously determined by its defect transition level and concentration. A dopant with shallow defect transition level will be more efficient to donate carriers than that with deep defect transition level under the same doping concentration. Mn and Ni have low carrier donation efficiency in β-FeSi$_2$ due to their relatively deep defect transition levels (see Figure 1a, such as 0.30 eV above the valence band maximum for Mn).[31] Thus, even though their doping concentration is as high as 10%, the doped samples still possess low carrier concentrations as mentioned above. On the other hand, β-FeSi$_2$ has intrinsically high κ_L, with the values of higher than 12 W m^{-1} K^{-1} at 300 K.[9,32,33] Although doping external elements can strengthen the phonon scattering, the κ_L values for the doped systems are still much higher than those for the state-of-the-art TE materials.[26−30,34−37]

On the basis of the first-principles calculations, we find that Al has a much shallower defect acceptor transition level (see Figure 1a, 0.15 eV below the valence band maximum) in β-FeSi$_2$ than Mn. This indicates that Al would be a more efficient p-type dopant with higher carrier donation efficiency to enhance the carrier concentration and optimize the electrical transport performance of β-FeSi$_2$ than Mn. Guided by this calculation, a series of Al-doped β-FeSi$_2$ compounds have been first prepared to optimize the electrical transport performance. Then, the heavy element Os is further alloyed in FeSi$_{1.96}$Al$_{0.04}$ to suppress the κ_L. Because of the synergistically optimized electrical and thermal transports, a maximum zT of 0.35 is obtained for p-type Fe$_{0.80}$Os$_{0.20}$Si$_{1.96}$Al$_{0.04}$, which doubles that of the highest value for p-type β-FeSi$_2$ materials reported before (see Figure 1b).

2. EXPERIMENTAL SECTION

2.1. Sample Preparation. Polycrystalline FeSi$_2$-based samples were synthesized from high purity elements Fe (Alfa Aesar, 99.98%, granules), Os (Alfa Aesar, 99.95%, powders), Al (Alfa Aesar, 99.99%, shots), Mn (Alfa Aesar, 99.95%, pieces), and Si (Alfa Aesar, 99.99%, granules). They were weighed out in the atomic ratio of FeSi$_{2-x}$Al$_x$ (x = 0, 0.02, 0.03, 0.04, 0.05, and 0.07), Fe$_{1-y}$Mn$_y$Si$_2$ (y = 0, 0.02, 0.04,

0.06, 0.08, and 0.10), and Fe$_{1-z}$Os$_z$Si$_{1.96}$Al$_{0.04}$ (z = 0, 0.05, 0.10, 0.15, and 0.20) and then melted in an argon atmosphere. The ingots were manually grounded into fine powders and sintered at 1223 K for 10 min under a uniaxial pressure of 65 MPa by spark plasma sintering (Sumitomo, SPS-2040). The as-sintered samples were sealed in silica tubes under vacuum, annealed at 1173 K for 5 days, and then naturally cooled to room temperature. The purpose of this postannealing process is to let the α-FeSi$_{2+\delta}$ phase and ε-FeSi phase in the as-sintered samples sufficiently react to form the final β-FeSi$_2$ phase. High relative densities above 95% were obtained for all bulks.

2.2. Structural Characterization. The phase structure was identified by the X-ray diffraction analysis (XRD, Cu Kα, λ = 1.5418 Å, Rigaku D/max 2550 V). The measurements were performed in the 2θ range of 15°−75° with a step size of 0.02°. The chemical composition and element homogeneity were determined by field emission scanning electron microscopy (FESEM, ZEISS Supra 55) and energy dispersive X-ray analysis (EDS, Oxford) by using an acceleration voltage of 20 kV.

2.3. TE Properties. The electrical conductivity (σ) and Seebeck coefficient (S) were concurrently measured by using a ZEM-3 (Ulvac-Riko) under a helium atmosphere. The thermal diffusivity (D) was measured by using the laser flash method in an argon atmosphere (Netzsch, LFA-457). The heat capacity (C_p) was estimated according to the Dulong−Petit approximation ($C_p = 3Nk_B$). The density (d) was determined by the Archimedes method. The thermal conductivity (κ) was calculated from $\kappa = DC_pd$. The Hall coefficient (R_H) was measured at 5−300 K by the physical property measurement system (PPMS, Quantum Design, San Diego, CA). The Hall carrier concentration (p_H) was estimated to be equal to $1/R_He$, where e is the elementary charge, and the Hall carrier mobility (μ_H) was calculated according to the relationship $\mu_H = R_H\sigma$. The estimated measurement accuracies for electrical conductivity, Seebeck coefficient, and thermal diffusion were around 3, 5, and 7%, respectively.

2.4. Computational Methods. The defect transition level of Al was calculated based on the density functional theory (DFT) using the Vienna *ab initio* simulation package (VASP).[42,43] The projector augmented wave (PAW) method was implemented to describe the core electrons, and the SCAN exchange-correlation functional was adopted for the generalized gradient approximation (GGA).[44,45] The cutoff energy was set to 22.5 Ry for the plane-wave basis. A 96-atom supercell was employed to model the defects. The 2 × 2 × 2 k-point meshes were used for sampling the Brillouin zone.[46] The atomic structures were fully optimized until the convergence criteria of energy was <1 × 10^{-6} Ry and the Hellmann−Feynman force on all atoms was smaller than 5 × 10^{-4} Ry/bohr. The defect transition level (or activation energy) of a point defect for a transition from charge state q to q' is defined as follows:[47,48]

$$\varepsilon(q/q') = \frac{E_D^q - E_D^{q'}}{q - q'} - E_{VBM}$$

(1)
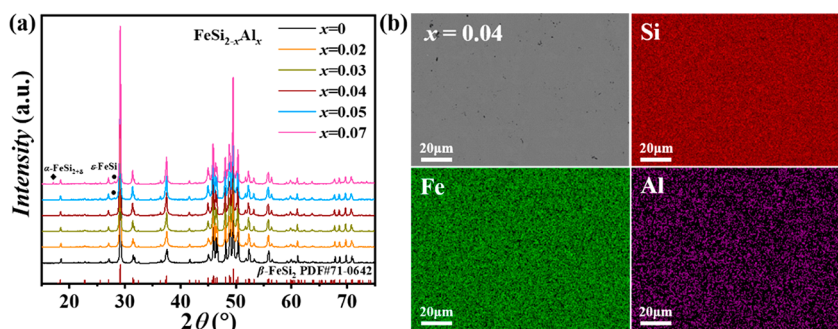
Figure 2. (a) Room-temperature powder X-ray diffraction patterns (PXRD) for $FeSi_{2-x}Al_x$ (x = 0, 0.02, 0.03, 0.04, 0.05, and 0.07). (b) Backscattered electron microscopy (BSE) image and elemental mappings for $FeSi_{1.96}Al_{0.04}$.
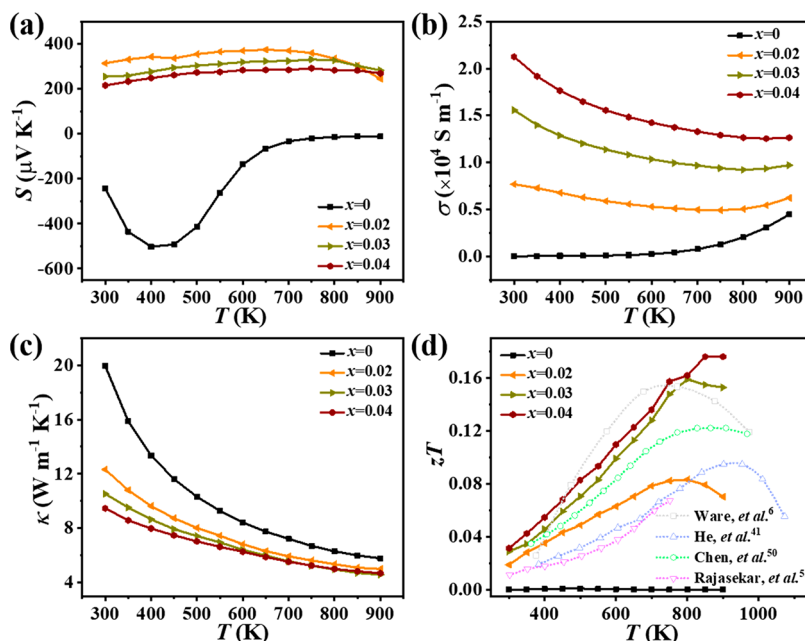
Figure 3. Temperature dependences of (a) Seebeck coefficient S, (b) electrical conductivity σ, (c) thermal conductivity κ, and (d) TE figure of merit zT for $FeSi_{2-x}Al_x$ (x = 0, 0.02, 0.03, and 0.04). The data of some Al-doped $FeSi_2$ compounds reported previously are also included for comparison.[6,41,50,51]

Here, E_D^q is the total energy of the supercell with a point defect of charge q. E_{VBM} is the energy of the valence band maximum (VBM).

3. RESULTS AND DISCUSSION

Figure 2a shows the room-temperature powder X-ray diffraction patterns (PXRD) of polycrystalline $FeSi_{2-x}Al_x$ (x = 0, 0.02, 0.03, 0.04, 0.05, and 0.07) samples. When the Al-doping concentration $x \leq 0.04$, all diffraction peaks can be well identified belonging to the orthorhombic structure of β-$FeSi_2$ (*Cmca*, PDF#71-0642). No diffraction peaks belonging to the secondary phases are detected. With further increasing the Al-doping concentration to 0.05 and 0.07, new diffraction peaks are detected at 2θ = 17.2° and 2θ = 27.9°, which are indexed to α-$FeSi_{2+\delta}$ and ε-FeSi, respectively. This suggests that the maximum solution limit of Al in β-$FeSi_2$ to maintain pure phase is around 0.04, which is consistent with the scanning electron microscopy (SEM) analysis. As shown in Figure 2b, all elements are homogeneously distributed inside the $FeSi_{1.96}Al_{0.04}$. No elemental agglomeration is observed. However, obvious elemental agglomeration is observed for $FeSi_{1.95}Al_{0.05}$ and $FeSi_{1.93}Al_{0.07}$ (see Figure S1).

Figure 3 shows the measured TE properties for $FeSi_{2-x}Al_x$ (x = 0, 0.02, 0.03, and 0.04). Because there are secondary phases in $FeSi_{1.95}Al_{0.05}$ and $FeSi_{1.93}Al_{0.07}$, their TE properties are not shown here. The pristine $FeSi_2$ shows a negative Seebeck coefficient (S) throughout the measured temperature range. The turn point around 400 K is related to the transition from impurity band conduction to polaron conduction.[49] Doping Al in $FeSi_2$ changes the sign of S from negative into positive. This indicates that the holes are the dominant carries for these $FeSi_{2-x}Al_x$ samples. This is reasonable because Al is on the left side of Si in the periodic table and it acts as acceptor dopant in β-$FeSi_2$. The S values for $FeSi_{2-x}Al_x$ are in the range 200−300 μV K^{-1} at 300 K, which are quite high values as compared to those for the state-of-the-art TE materials. The turn point of S around 750 K should be related to the intrinsic excitation. Doping Al in β-$FeSi_2$ significantly enhances the electrical conductivity (σ). As shown in Figure 3b, the σ for the pristine $FeSi_2$ is 16.9 S m^{-1} at 300 K. It is gradually increased to 4.4 × 10^3 S m^{-1} at 900 K due to the thermal excitation of carriers from the valence band to the conduction band. However, when the Al-doping concentration is 0.02, the σ is already increased to 7.7 × 10^3 S m^{-1} at 300 K, even higher than that for the
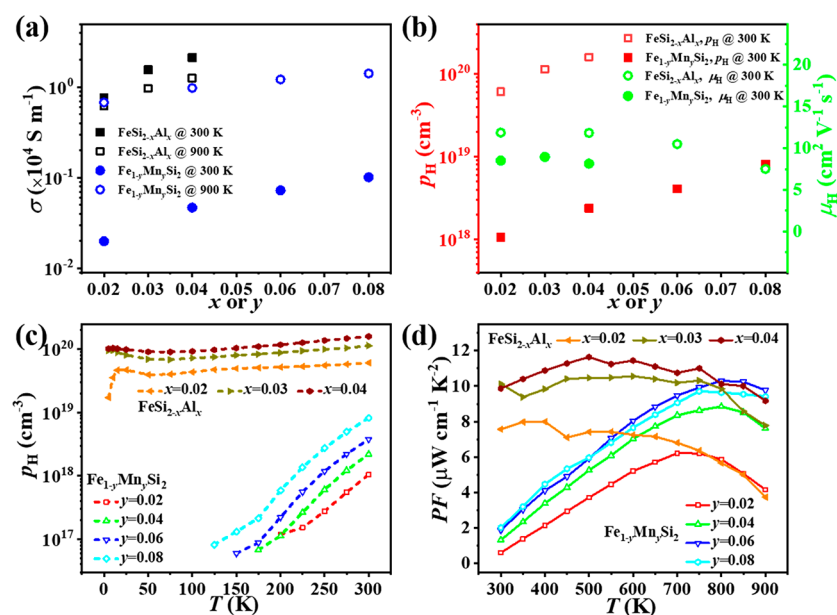
Figure 4. (a) Electrical conductivity σ at 300 and 900 K, (b) room temperature carrier concentration p_H, and carrier mobility μ_H as a function of doping concentration for $FeSi_{2-x}Al_x$ (x = 0.02, 0.03, and 0.04). Temperature dependences of (c) Hall carrier concentration p_H and (d) power factor PF for $FeSi_{2-x}Al_x$ (x = 0.02, 0.03, and 0.04). The data for $Fe_{1-y}Mn_ySi_2$ (y = 0.02, 0.04, 0.06, and 0.08) are included for comparison.

pristine $FeSi_2$ at 900 K. Further increasing the Al-doping concentration can yield higher σ throughout the entire measured temperature range. When the Al-doping concentration is 0.04, the σ is increased to 2.1 × 10^4 S m^{-1} at 300 K, about 3 orders of magnitude enhancement as compared with that for the pristine $FeSi_2$ at 300 K.

Figure 3c displays the total thermal conductivity (κ) as a function of temperature for all $FeSi_{2-x}Al_x$ samples. The κ decreases with increasing temperature, suggesting that the Umklapp process dominates the thermal transports. The κ for the pristine $FeSi_2$ at 300 K is 19.9 W m^{-1} K^{-1}. It is reduced to 9.5 W m^{-1} K^{-1} when the Al-doping concentration is 0.04, about 52% reduction. However, above 700 K, the reduction is not so obvious. For example, the κ at 900 K for the pristine $FeSi_2$ is 5.8 W m^{-1} K^{-1}, while that for $FeSi_{1.96}Al_{0.04}$ is 4.7 W m^{-1} K^{-1}. The reduction is only about 19%. Because the carrier thermal conductivity (κ_e) is in proportion to the σ based on the Wiedemann−Franz law, the κ_e would increase upon Al doping. Then, the above κ reductions mainly originate from the suppressed lattice thermal conductivity (κ_L). Combining the measured S, σ, and κ, the zT is calculated for all $FeSi_{2-x}Al_x$ samples; a maximum zT of 0.18 is achieved for $FeSi_{1.96}Al_{0.04}$ at 850 K. This value is comparable with the best result for p-type β-$FeSi_2$ reported previously (see Figure 1b).

Previously, Mn was the most common p-type dopant for β-$FeSi_2$.[21−23] The biggest differences between Mn-doped β-$FeSi_2$ and the present Al-doped β-$FeSi_2$ lie in the σ and its temperature dependence. Figure 4a summarizes the σ values for Al- and Mn-doped β-$FeSi_2$ at 300 and 900 K. Clearly, the σ values at 300 K for Al-doped β-$FeSi_2$ samples are 1−2 orders of magnitude higher than those for Mn-doped β-$FeSi_2$. Likewise, as shown in Figure 3b, the σ for Al-doped β-$FeSi_2$ decreases with increasing temperature, showing typical heavily doped degenerate semiconducting behavior. However, the σ for Mn-doped β-$FeSi_2$ increases with increasing temperature, showing intrinsic semiconducting behavior (see Figure S2a) despite that the Mn-doping concentration in β-$FeSi_2$ is already as high as 0.08. The same intrinsic semiconducting behavior has been

also observed for n-type Co- and Ni-doped β-$FeSi_2$ samples.[25] This reverse temperature dependence is the reason why the σ for the Al- and Mn-doped systems are quite different at 300 K, but similar at 900 K.

The σ can be given by the formula $\sigma = p_H e\mu_H$, where p_H is the Hall carrier concentration, e is the elemental charge, and μ_H is the Hall carrier mobility. Figure 4b shows the p_H and μ_H for Al-and Mn-doped β-$FeSi_2$ at 300 K. It can be seen that the p_H values are quite different between these two systems, while the μ_H values are comparable. This indicates that the p_H is responsible for the hugely different σ shown in Figure 4a. The carrier concentration p of a doped semiconductor is related to the efficiency of the donor to donate carriers, which is further determined by the position of donor's defect transition level and the temperature according to the equation[52]

$$p = (N_v N_a)^{1/2} e^{-E_a/2k_BT} \qquad (2)$$

where N_v is the valence band density, N_a is the concentration of defects, E_a is the activation energy of defect transition level, and k_B is the Boltzmann constant. E_a quantitatively reflects the position of the defect transition level. The donor with small E_a (i.e., shallower defect transition level) is easier to be ionized to donate carriers. As shown in Figure 1a, the calculated defect transition level for Al already enters into the valence band, indicating that the E_a for Al dopant is very small. Thus, the Al dopant is very easy to be ionized. This can be confirmed by the measured p_H below 300 K. As shown in Figure 4c, the p_H for Al-doped β-$FeSi_2$ samples is almost temperature-independent, indicating that the Al dopant has been completely ionized at very low temperature. However, the case is different for Mn-doped β-$FeSi_2$. Because the Mn dopant has deep defect transition level (E_a = 0.3 eV), it can only be completely ionized until the temperature is raised to very high. According to eq 2, before the completely ionization, the p_H values for Mn-doped β-$FeSi_2$ would demonstrate strong temperature dependence. This is consistent with the scenario shown in Figure 4c that the
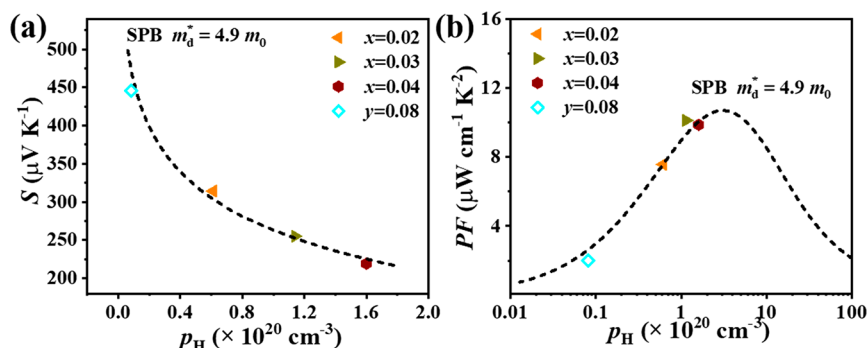
Figure 5. (a) Seebeck coefficient S and (b) power factor PF as a function of Hall carrier concentration p_H at 300 K for $FeSi_{2-x}Al_x$ (x = 0.02, 0.03, and 0.04). The short dashed lines are calculated on the basis of the SPB model using $m_d^* = 4.9m_0$. The data for $Fe_{0.92}Mn_{0.08}Si_2$ is also included for comparison.
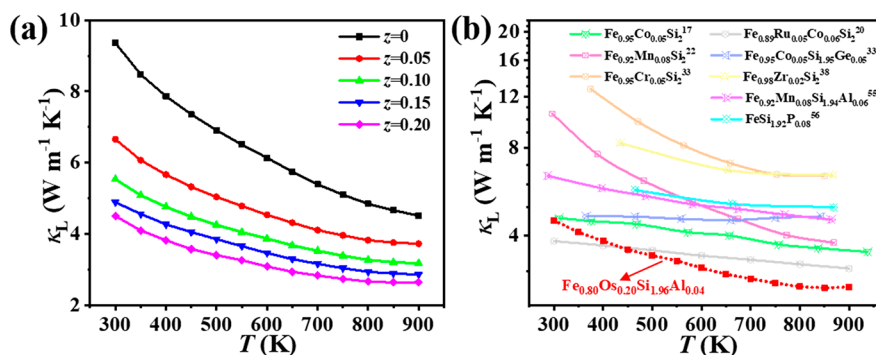
Figure 6. (a) Lattice thermal conductivity κ_L as a function of temperature for $Fe_{1-z}Os_zSi_{1.96}Al_{0.04}$ (z = 0, 0.05, 0.10, 0.15, and 0.20). (b) Comparison of the κ_L for several β-$FeSi_2$-based compounds previously reported[17,20,33,38,55,56] and $Fe_{0.80}Os_{0.20}Si_{1.96}Al_{0.04}$ in this work.

p_H values quickly increase by 2 orders of magnitude from 150 to 300 K.

The significantly enhanced σ caused by Al-doping greatly improves the power factor (PF). As shown in Figure 4d, the PF increases with increasing the Al-doping concentration throughout the entire measured temperature range. Particularly, the Al-doped β-$FeSi_2$ samples possess high PF values at low temperature range. For example, the PF for $FeSi_{1.96}Al_{0.04}$ is 9.9 $\mu W\ cm^{-1}\ K^{-2}$ at 300 K, which is about 4.9 times than that for $Fe_{0.92}Mn_{0.08}Si_2$ at the same temperature. Actually, this PF value is even equivalent to that of $Fe_{0.92}Mn_{0.08}Si_2$ at high temperatures.

The single parabolic band (SPB) model is widely adopted to predict the theoretical maximum PF for TE materials.[53] Based on the Fermi statistics, the Seebeck coefficient and Hall carrier concentration can be described as follows:

$$S = \frac{k_B}{e}\left[\frac{(2+\lambda)F_{\lambda+1}(\eta)}{(1+\lambda)F_\lambda(\eta)} - \eta\right] \tag{3}$$

$$p_H = \frac{p}{r_H} \tag{4}$$

$$p = 4\pi\left(\frac{2m_d^*k_BT}{h^2}\right)^{3/2}F_{1/2}(\eta) \tag{5}$$

$$r_H = \frac{3}{4}\frac{F_{1/2}(\eta)F_{-1/2}(\eta)}{F_0^2(\eta)} \tag{6}$$

where λ is the scattering factor with a value of 0 for acoustic phonons scattering based on our Hall carrier mobility data (see

Figure S3), m_d^* is the density-of-state effective mass, h is the Planck constant, and η ($= E_F/k_BT$) is the reduced Fermi level. The Fermi integrals are given by $F_m(\eta) = \int_0^\infty \frac{x^m\,dx}{1+\exp(x-\eta)}$, where x is the reduced carrier energy. Figure 5a shows the calculated Pisarenko plot (S vs p_H) at 300 K based on the SPB model with the density-of-state effective mass $m_d^* = 4.9m_0$, where m_0 is the effective mass of free electron. This calculated plot well interprets the experimental data for the Al-doped β-$FeSi_2$ samples and $Fe_{0.92}Mn_{0.08}Si_2$, suggesting that these samples have similar band structure near the Fermi level. By using $m_d^* = 4.9m_0$, we further calculate the relationship between PF and p_H at room temperature. As shown in Figure 5b, the optimal carrier concentration corresponding to the theoretical maximum PF for p-type β-$FeSi_2$ is around $2.5 \times 10^{20}\ cm^{-3}$ at room temperature. Because the maximum p_H for the present Al-doped β-$FeSi_2$ is already quite close to the optimal carrier concentration, the room for PF enhancement is already very narrow. Thus, further improving the zT of p-type Al-doped β-$FeSi_2$ should focus on suppressing its lattice thermal conductivity κ_L.

Here, we alloy the heavy element Os at the Fe sites of $FeSi_{1.96}Al_{0.04}$ with the purpose to further improve the zT. As shown in Figure S4, all the $Fe_{1-z}Os_zSi_{1.96}Al_{0.04}$ (z = 0, 0.05, 0.10, 0.15, and 0.20) samples possess similar X-ray diffraction patterns. No impurity diffraction peaks are observed. These suggest that Al and Os codoped materials crystallize in the same orthogonal structure with the pristine β-$FeSi_2$. Figure 6a shows the κ_L calculated by subtracting the carrier thermal conductivity κ_e from the total κ. The κ_e shown in Figure S5 is calculated by the Wiedemann–Franz law ($\kappa_e = L\sigma T$, where L is
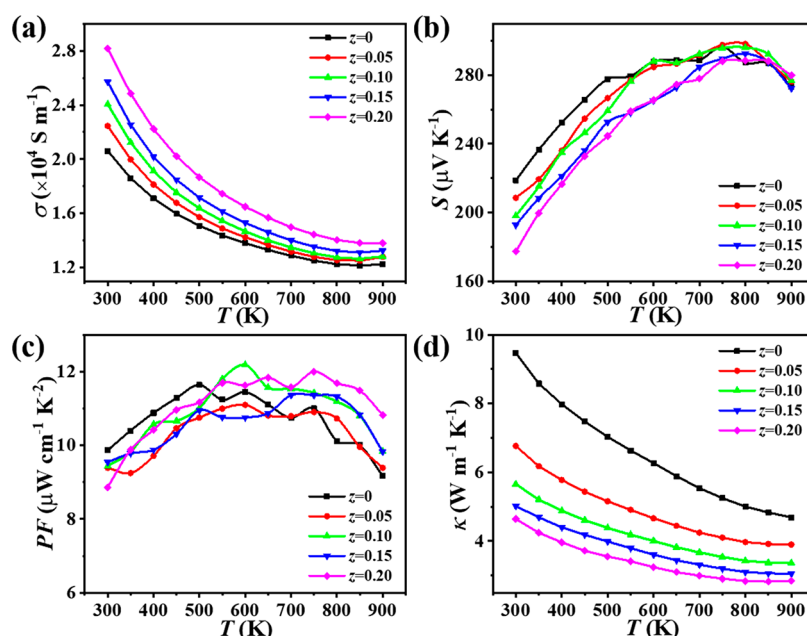
Figure 7. (a) Temperature dependences of (a) electrical conductivity σ, (b) Seebeck coefficient S, (c) power factor PF, and (d) thermal conductivity κ for $Fe_{1-z}Os_zSi_{1.96}Al_{0.04}$ (z = 0, 0.05, 0.10, 0.15, and 0.20).

the Lorenz number). In this study, the L values are estimated according to the empirical formula expressed by $L = 1.5 + e^{-|S|/116}$.[54] The data are shown in Figure S6. It can be seen that the effect of Os on the κ_L reduction is very obvious. As shown in Figure 6a, the κ_L decreases with increasing the Os-alloying concentration in the entire measured temperature range. The κ_L for $Fe_{0.80}Os_{0.20}Si_{1.96}Al_{0.04}$ is 4.5 W m^{-1} K^{-1} at 300 K, about 52% reduction as compared with that for the $FeSi_{1.96}Al_{0.04}$. The κ_L monotonously decreases with increasing temperature. At 900 K, the κ_L is 2.6 W m^{-1} K^{-1} for $Fe_{0.80}Os_{0.20}Si_{1.96}Al_{0.04}$, about 41% of $FeSi_{1.96}Al_{0.04}$ and 53% of the pristine $FeSi_2$. As shown in Figure 6b, this value is already the lowest value among the data reported previously for doped β-$FeSi_2$ systems. Os has a quite heavier atomic mass and a larger atomic radius than Fe. Alloying Os at the Fe sites would generate strong point defect scattering to interrupt the normal transport of high-frequency lattice phonons. These are responsible for the low κ_L present above.

Beyond the κ_L, alloying Os in $FeSi_{1.96}Al_{0.04}$ also alters the electrical transport properties. Figure 7a shows the σ for $Fe_{1-z}Os_zSi_{1.96}Al_{0.04}$ (z = 0, 0.05, 0.10, 0.15, and 0.20). All Os-alloyed samples still demonstrate the typical heavily doped degenerate semiconducting behavior, with the σ decreasing with increasing temperature. Alloying Os improves the σ in the entire measured temperature range. The σ is 2.8 × 10^4 S m^{-1} for $Fe_{0.80}Os_{0.20}Si_{1.96}Al_{0.04}$ at 300 K, about 33% enhancement as compared with the $FeSi_{1.96}Al_{0.04}$. Likewise, the S is decreased by Os alloying. The S for $Fe_{0.80}Os_{0.20}Si_{1.96}Al_{0.04}$ is 177.4 μV K^{-1} at 300 K, about 18% reduction as compared with that for the $FeSi_{1.96}Al_{0.04}$.

The variations of S and σ shown in Figure 7 are related to the increase of carrier concentration. As shown in Table 1, the p_H increases with increasing the Os-alloying concentration. $Fe_{0.80}Os_{0.20}Si_{1.96}Al_{0.04}$ has a maximum p_H value of 1.9 × 10^{20} cm^{-3} at 300 K, about 17% enhancement as compared with $FeSi_{1.96}Al_{0.04}$. Likewise, the μ_H also increases with increasing Os-alloying concentration. Figure S7 plots the S as a function of p_H at 300 K for $Fe_{1-z}Os_zSi_{1.96}Al_{0.04}$ (z = 0, 0.05, 0.10, 0.15,

Table 1. Transport Properties of $Fe_{1-z}Os_zSi_{1.96}Al_{0.04}$ (z = 0, 0.05, 0.10, 0.15, and 0.20) at Room Temperature

nominal composition	σ (10^4 S m^{-1})	S (μV K^{-1})	n_H (10^{20} cm^{-3})	μ_H (cm^2 V^{-1} s^{-1})
$FeSi_{1.96}Al_{0.04}$	2.1	218.8	1.6	8.1
$Fe_{0.95}Os_{0.05}Si_{1.96}Al_{0.04}$	2.3	208.6	1.7	8.5
$Fe_{0.90}Os_{0.10}Si_{1.96}Al_{0.04}$	2.4	198.1	1.7	8.8
$Fe_{0.85}Os_{0.15}Si_{1.96}Al_{0.04}$	2.6	192.7	1.8	9.2
$Fe_{0.80}Os_{0.20}Si_{1.96}Al_{0.04}$	2.8	177.4	1.9	9.4

and 0.20). The data for $FeSi_{2-x}Al_x$ (x = 0.02, 0.03, and 0.04) are also included for comparison. It can be seen that the data for $Fe_{1-z}Os_zSi_{1.96}Al_{0.04}$ obviously deviate off the calculated Pisarenko plot at 300 K based on the SPB model with m_d^* = 4.9m_0. This indicates that alloying Os in $FeSi_{1.96}Al_{0.04}$ modifies the band structure near the Fermi level and changes the m_d^*.

Based on the measured σ and S, the PF is calculated. As presented in Figure 7c, all samples possess comparable PF in the entire measured temperature range. No obvious PF deterioration is observed due to Os-alloying. Figure 7d shows the total thermal conductivity κ for $Fe_{1-z}Os_zSi_{1.96}Al_{0.04}$ (z = 0, 0.05, 0.10, 0.15, and 0.20). Alloying Os significantly reduces the κ. Because the σ for all samples is on the order of 10^4 S m^{-1}, the contribution of κ_e to the κ is very low. As shown in Figure S5, the maximum κ_e for $Fe_{1-z}Os_zSi_{1.96}Al_{0.04}$ is only 0.2 W m^{-1} K^{-1} at 900 K, about 7% of the κ. Thus, although the increased σ leads to higher κ_e, the κ still decreases with increasing the Os-alloying concentration.

Finally, the zT values for $Fe_{1-z}Os_zSi_{1.96}Al_{0.04}$ (z = 0, 0.05, 0.10, 0.15, and 0.20) are calculated and plotted in Figure 8a. Because of the well-maintained PF and significantly reduced κ_L, the zT is boosted up in the entire measured temperature range. The peak zT is 0.35 for $Fe_{0.80}Os_{0.20}Si_{1.96}Al_{0.04}$ at 850 K, which is about 2 times that for the Os-free $FeSi_{1.96}Al_{0.04}$. Figure 1b summarizes the zT values for typical p-type β-$FeSi_2$-based compounds reported previously. It can be seen that the zT in our work is double that of the highest value reported
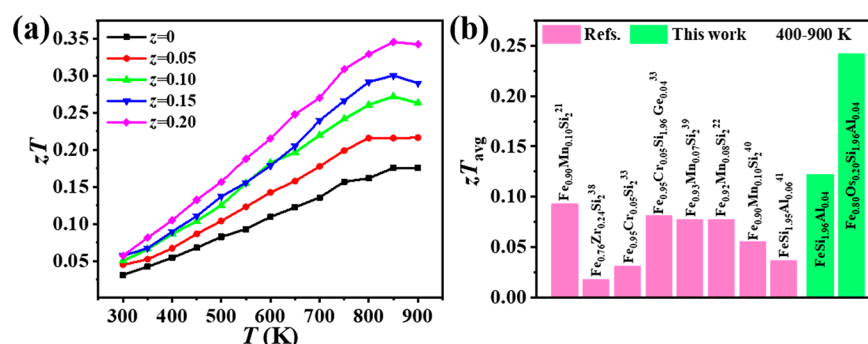
Figure 8. (a) Temperature dependence of TE figure of merit zT for $Fe_{1-z}Os_zSi_{1.96}Al_{0.04}$ ($z = 0$, 0.05, 0.10, 0.15, and 0.20). (b) Comparison of the average TE figure of merit (zT_{avg}) at 400−900 K for $FeSi_{1.96}Al_{0.04}$, $Fe_{0.80}Os_{0.20}Si_{1.96}Al_{0.04}$, and several p-type β-$FeSi_2$ compounds previously reported.[21,22,33,38−41]

previously. More importantly, the zT enhancement occurs in the entire temperature range. This leads to more significantly enhanced average zT (zT_{avg}), which is also doubled comparing with that of the highest value reported previously, as demonstrated in Figure 8b. Thus, the present Os-alloyed $FeSi_{2-x}Al_x$ samples would be more suitable to be fabricated into efficient TE device than the Mn-doped samples.

4. CONCLUSION

To sum up, via doping Al which has the shallow acceptor transition level in β-$FeSi_2$, we successfully optimize the electrical transport properties of β-$FeSi_2$ from 300 to 900 K. When the Al-doping concentration is 0.04, the PF is significantly improved to 9.9 $\mu W\ cm^{-1}\ K^{-2}$ at 300 K, close to the theoretical maximum value predicted by the SPB model. The $FeSi_{1.96}Al_{0.04}$ shows a peak zT of 0.18 at 850 K. Alloying Os in $FeSi_{1.96}Al_{0.04}$ can further reduce the κ_L. When the Os-alloying concentration is 0.20, the κ_L reaches a minimum value of 2.6 W m^{-1} K^{-1} at 900 K. Meanwhile, alloying Os yields little deterioration on the PF. Finally, a maximal zT of 0.35 is obtained at 850 K for $Fe_{0.80}Os_{0.20}Si_{1.96}Al_{0.04}$, which doubles that of the highest value reported so far for p-type β-$FeSi_2$-based compounds (Figure 1b).

■ ASSOCIATED CONTENT

Ⓢ Supporting Information

The Supporting Information is available free of charge at https://pubs.acs.org/doi/10.1021/acsami.0c00321.

BSE images and elemental mappings for $FeSi_{1.95}Al_{0.05}$ and $FeSi_{1.93}Al_{0.07}$; temperature dependences of electrical conductivity σ and Seebeck coefficient S for $Fe_{1-y}Mn_ySi_2$; temperature dependences of Hall carrier mobility μ_H for $FeSi_{2-x}Al_x$ and $Fe_{1-y}Mn_ySi_2$; XRD results of $Fe_{1-z}Os_zSi_{1.96}Al_{0.04}$; carrier thermal conductivity κ_e for $Fe_{1-z}Os_zSi_{1.96}Al_{0.04}$; Lorenz number L for $Fe_{1-z}Os_zSi_{1.96}Al_{0.04}$; Seebeck coefficient S as a function of Hall carrier concentration p_H at 300 K for $Fe_{1-z}Os_zSi_{1.96}Al_{0.04}$ and $FeSi_{2-x}Al_x$ (PDF)

■ AUTHOR INFORMATION

Corresponding Authors

Pengfei Qiu − *State Key Laboratory of High Performance Ceramics and Superfine Microstructure, Shanghai Institute of Ceramics, Chinese Academy of Sciences, Shanghai 200050, China;* ⓞ orcid.org/0000-0001-6011-1210; Email: qiupf@mail.sic.ac.cn

Xun Shi − *State Key Laboratory of High Performance Ceramics and Superfine Microstructure, Shanghai Institute of Ceramics, Chinese Academy of Sciences, Shanghai 200050, China;* ⓞ orcid.org/0000-0002-8086-6407; Email: xshi@mail.sic.ac.cn

Authors

Xiaolong Du − *State Key Laboratory of High Performance Ceramics and Superfine Microstructure, Shanghai Institute of Ceramics, Chinese Academy of Sciences, Shanghai 200050, China; Center of Materials Science and Optoelectronics Engineering, University of Chinese Academy of Sciences, Beijing 100049, China*

Jun Chai − *State Key Laboratory of High Performance Ceramics and Superfine Microstructure, Shanghai Institute of Ceramics, Chinese Academy of Sciences, Shanghai 200050, China; Center of Materials Science and Optoelectronics Engineering, University of Chinese Academy of Sciences, Beijing 100049, China*

Tao Mao − *State Key Laboratory of High Performance Ceramics and Superfine Microstructure, Shanghai Institute of Ceramics, Chinese Academy of Sciences, Shanghai 200050, China; Center of Materials Science and Optoelectronics Engineering, University of Chinese Academy of Sciences, Beijing 100049, China*

Ping Hu − *State Key Laboratory of High Performance Ceramics and Superfine Microstructure, Shanghai Institute of Ceramics, Chinese Academy of Sciences, Shanghai 200050, China; Center of Materials Science and Optoelectronics Engineering, University of Chinese Academy of Sciences, Beijing 100049, China*

Jiong Yang − *Materials Genome Institute, Shanghai University, Shanghai 200444, China;* ⓞ orcid.org/0000-0002-5862-5981

Yi-Yang Sun − *State Key Laboratory of High Performance Ceramics and Superfine Microstructure, Shanghai Institute of Ceramics, Chinese Academy of Sciences, Shanghai 200050, China;* ⓞ orcid.org/0000-0002-0356-2688

Lidong Chen − *State Key Laboratory of High Performance Ceramics and Superfine Microstructure, Shanghai Institute of Ceramics, Chinese Academy of Sciences, Shanghai 200050, China; Center of Materials Science and Optoelectronics Engineering, University of Chinese Academy of Sciences, Beijing 100049, China*

Complete contact information is available at:
https://pubs.acs.org/10.1021/acsami.0c00321

Notes

The authors declare no competing financial interest.

■ REFERENCES

(1) He, J.; Tritt, T. M. Advances in Thermoelectric Materials Research: Looking Back and Moving Forward. *Science* **2017**, *357*, No. eaak9997.

(2) Shi, X.; Chen, L. D. Thermoelectric Materials Step Up. *Nat. Mater.* **2016**, *15*, 691−692.

(3) Tan, G. J.; Zhao, L. D.; Kanatzidis, M. G. Rationally Designing High-Performance Bulk Thermoelectric Materials. *Chem. Rev.* **2016**, *116*, 12123−12149.

(4) Zhu, T. J.; Liu, Y. T.; Fu, C. G.; Heremans, J. P.; Snyder, J. G.; Zhao, X. B. Compromise and Synergy in High-Efficiency Thermoelectric Materials. *Adv. Mater.* **2017**, *29*, 1605884.

(5) Chang, C.; Zhao, L. D. Anharmoncity and Low Thermal Conductivity in Thermoelectrics. *Mater. Today Phys.* **2018**, *4*, 50−57.

(6) Ware, R. M.; McNeill, D. J. Iron Disilicide as a Thermoelectric Generator Material. *Proc. Inst. Electr. Eng.* **1964**, *111*, 178−182.

(7) Arushanov, E.; Lisunov, K. G. Transport Properties of β-FeSi$_2$. *Jpn. J. Appl. Phys.* **2015**, *54*, 07JA02.

(8) Nozariasbmarz, A.; Agarwal, A.; Coutant, Z. A.; Hall, M. J.; Liu, J.; Liu, R.; Malhotra, A.; Norouzzadeh, P.; Öztürk, M. C.; Ramesh, V. P.; Sargolzaeiaval, Y.; Suarez, F.; Vashaee, D. Thermoelectric Silicides: A Review. *Jpn. J. Appl. Phys.* **2017**, *56*, 05DA04.

(9) Liu, N. M.; Jensen, W. A.; Zebarjadi, M.; Floro, J. A. Tunable β-FeSi$_2$-Si$_{1-y}$Ge$_y$ Nanocomposites by a Novel React/Transform Spark Plasma Sintering Approach for Thermoelectric Applications. *Mater. Today Phys.* **2018**, *4*, 19−27.

(10) Inoue, H.; Kobayashi, T.; Kato, M.; Yoneda, S. A Low-Cost Production Method of FeSi$_2$ Power Generation Thermoelectric Modules. *J. Electron. Mater.* **2016**, *45*, 1767−1771.

(11) Dusausoy, Y.; Protas, J.; Wandji, R.; Roques, B. Structure Cristalline du Disiliciure de Fer, FeSi$_2\beta$. *Acta Crystallogr., Sect. B: Struct. Crystallogr. Cryst. Chem.* **1971**, *27*, 1209−1218.

(12) Katsumata, H.; Makita, Y.; Kobayashi, N.; Shibata, H.; Hasegawa, M.; Aksenov, I.; Kimura, S.; Obara, A.; Uekusa, S. i. Optical Absorption and Photoluminescence Studies of β-FeSi$_2$ Prepared by Heavy Implantation of Fe$^+$ Ions into Si. *J. Appl. Phys.* **1996**, *80*, 5955−5962.

(13) Mohd Redzuan, F. L. B.; Ito, M.; Takeda, M. Phosphorus Doping in n-Type β-FeSi$_2$/Si Composites and Its Effects on Thermoelectric Properties. *Intermetallics* **2019**, *108*, 19−24.

(14) Liu, N. M.; Rezaei, S. E.; Jensen, W. A.; Song, S. W.; Ren, Z. F.; Esfarjani, K.; Zebarjadi, M.; Floro, J. A. Improved Thermoelectric Performance of Eco-Friendly β-FeSi$_2$-SiGe Nanocomposite via Synergistic Hierarchical Structuring, Phase Percolation, and Selective Doping. *Adv. Funct. Mater.* **2019**, *29*, 1903157.

(15) Stöhrer, U.; Voggesberger, R.; Wagner, G.; Birkholz, U. Sintered FeSi$_2$ for Thermoelectric Power Generation. *Energy Convers. Manage.* **1990**, *30*, 143−147.

(16) Zhang, Z. H.; Zhang, C.; Wang, W. L.; Xie, J. X. Preparation of Bulk β-FeSi$_2$ by Synthetical Control of Melt Cyclical Superheating, Solidification and Cooling Process. *Intermetallics* **2014**, *49*, 143−148.

(17) Tani, J.-i.; Kido, H. Thermoelectric Properties of β-Fe$_{1-x}$Co$_x$Si$_2$ Semiconductors. *Jpn. J. Appl. Phys.* **2001**, *40*, 3236.

(18) Chen, H. Y.; Zhao, X. B.; Stiewe, C.; Platzek, D.; Mueller, E. Microstructures and Thermoelectric Properties of Co-Doped Iron Disilicides Prepared by Rapid Solidification and Hot Pressing. *J. Alloys Compd.* **2007**, *433*, 338−344.

(19) Qu, X. R.; Lü, S. C.; Hu, J. M.; Meng, Q. Y. Microstructure and Thermoelectric Properties of β-FeSi$_2$ Ceramics Fabricated by Hot-Pressing and Spark Plasma Sintering. *J. Alloys Compd.* **2011**, *509*, 10217−10221.

(20) Du, X. L.; Hu, P.; Mao, T.; Song, Q. F.; Qiu, P. F.; Shi, X.; Chen, L. D. Ru Alloying Induced Enhanced Thermoelectric Performance in FeSi$_2$-Based Compounds. *ACS Appl. Mater. Interfaces* **2019**, *11*, 32151−32158.

(21) Tani, J.-i.; Kido, H. Thermoelectric Properties of Mn-Doped β-FeSi$_2$ Fabricated by Spark Plasma Sintering. *J. Ceram. Soc. Jpn.* **2001**, *109*, 557−560.

(22) Zhao, X. B.; Chen, H. Y.; Müller, E.; Drasar, C. Thermoelectric Properties of Mn Doped FeSi$_x$ Alloys Hot-Pressed from Nitrided Rapidly Solidified Powders. *Appl. Phys. A: Mater. Sci. Process.* **2005**, *80*, 1123−1127.

(23) Sen, S.; Guha, P. K.; Banerji, P.; Pramanik, P. Mn and As Doping of β-FeSi$_2$ via a Chemical Method. *RSC Adv.* **2016**, *6*, 68238−68246.

(24) Komabayashi, M.; Hijikata, K.-i.; Ido, S. Effects of Some Additives on Thermoelectric Properties of FeSi$_2$ Thin Films. *Jpn. J. Appl. Phys.* **1991**, *30*, 331−334.

(25) Tani, J.-i.; Kido, H. Electrical Properties of Co-Doped and Ni-Doped β-FeSi$_2$. *J. Appl. Phys.* **1998**, *84*, 1408−1411.

(26) Li, J.; Zhang, X. Y.; Wang, X.; Bu, Z. L.; Zheng, L. T.; Zhou, B. Q.; Xiong, F.; Chen, Y.; Pei, Y. Z. High-Performance GeTe Thermoelectrics in Both Rhombohedral and Cubic Phases. *J. Am. Chem. Soc.* **2018**, *140*, 16190−16197.

(27) Shi, X. M.; Zhao, T. T.; Zhang, X. Y.; Sun, C.; Chen, Z. W.; Lin, S. Q.; Li, W.; Gu, H.; Pei, Y. Z. Extraordinary n-Type Mg$_3$SbBi Thermoelectrics Enabled by Yttrium Doping. *Adv. Mater.* **2019**, *31*, No. 1903387.

(28) Zhao, K. P.; Blichfeld, A. B.; Chen, H. Y.; Song, Q. F.; Zhang, T. S.; Zhu, C. X.; Ren, D. D.; Hanus, R.; Qiu, P. F.; Iversen, B. B.; Xu, F. F.; Snyder, G. J.; Shi, X.; Chen, L. D. Enhanced Thermoelectric Performance through Tuning Bonding Energy in Cu$_2$Se$_{1-x}$S$_x$ Liquid-Like Materials. *Chem. Mater.* **2017**, *29*, 6367−6377.

(29) Wan, S.; Qiu, P. F.; Huang, X. Y.; Song, Q. F.; Bai, S. Q.; Shi, X.; Chen, L. D. Synthesis and Thermoelectric Properties of Charge-Compensated S$_y$Pd$_x$Co$_{4-x}$Sb$_{12}$ Skutterudites. *ACS Appl. Mater. Interfaces* **2018**, *10*, 625−634.

(30) Yao, Z. C.; Li, W.; Tang, J.; Chen, Z. W.; Lin, S. Q.; Biswas, K.; Burkov, A.; Pei, Y. Z. Solute Manipulation Enabled Band and Defect Engineering for Thermoelectric Enhancements of SnTe. *InfoMat* **2019**, *1*, 571−581.

(31) Chai, J.; Ming, C.; Du, X. L.; Qiu, P. F.; Sun, Y. Y.; Chen, L. D. Thermodynamics, Kinetics and Electronic Properties of Point Defects in β-FeSi$_2$. *Phys. Chem. Chem. Phys.* **2019**, *21*, 10497−10504.

(32) Waldecker, G.; Meinhold, H.; Birkholz, U. Thermal Conductivity of Semiconducting and Metallic FeSi$_2$. *Phys. Status Solidi A* **1973**, *15*, 143−149.

(33) Kim, S. W.; Cho, M. K.; Mishima, Y.; Choi, D. C. High Temperature Thermoelectric Properties of P- and N-Type β-FeSi$_2$ with Some Dopants. *Intermetallics* **2003**, *11*, 399−405.

(34) Hao, F.; Qiu, P. F.; Tang, Y. S.; Bai, S. Q.; Xing, T.; Chu, H.-S.; Zhang, Q. H.; Lu, P.; Zhang, T. S.; Ren, D. D.; Chen, J. K.; Shi, X.; Chen, L. D. High Efficiency Bi$_2$Te$_3$-Based Materials and Devices for Thermoelectric Power Generation between 100 and 300 °C. *Energy Environ. Sci.* **2016**, *9*, 3120−3127.

(35) You, L.; Zhang, J. Y.; Pan, S. S.; Jiang, Y.; Wang, K.; Yang, J.; Pei, Y. Z.; Zhu, Q.; Agne, M. T.; Snyder, G. J.; Ren, Z. F.; Zhang, W. Q.; Luo, J. Realization of Higher Thermoelectric Performance by Dynamic Doping of Copper in n-Type PbTe. *Energy Environ. Sci.* **2019**, *12*, 3089−3098.

(36) Wang, C. L.; Lin, S. S.; Chen, H. Y.; Zhao, Y.; Zhao, L.; Wang, H. L.; Huo, D. X.; Chen, X. Y. Thermoelectric Performance of Si$_{80}$Ge$_{20-x}$Sb$_x$ Based Multiphase Alloys with Inhomogeneous Dopant Distribution. *Energy Convers. Manage.* **2015**, *94*, 331−336.

(37) Shi, X. L.; Liu, W. D.; Wu, A. Y.; Nguyen, V. T.; Gao, H.; Sun, Q.; Moshwan, R.; Zou, J.; Chen, Z. G. Optimization of Sodium

Hydroxide for Securing High Thermoelectric Performance in Polycrystalline $Sn_{1-x}Se$ via Anisotropy and Vacancy Synergy. *InfoMat* **2019**, DOI: 10.1002/inf2.12057.

(38) Ito, M.; Nagai, H.; Tahata, T.; Katsuyama, S.; Majima, K. Effects of Zr Substitution on Phase Transformation and Thermoelectric Properties of β-FeSi$_2$. *J. Appl. Phys.* **2002**, *92*, 3217−3222.

(39) Yamashita, O.; Tomiyoshi, S.; Sadatomi, N. Thermoelectric Properties of p- and n-Type FeSi$_2$ Prepared by Spray Drying, Compaction and Sintering Technique. *J. Mater. Sci.* **2003**, *38*, 1623−1629.

(40) Ito, M.; Takiguchi, Y. Thermoelectric Properties of p-Type $Fe_{0.9}Mn_{0.1}Si_2$ with Rare-Earth Oxide Addition. *Mater. Trans.* **2005**, *46*, 1497−1501.

(41) He, Z. M.; Platzek, D.; Stiewe, C.; Chen, H. Y.; Karpinski, G.; Müller, E. Thermoelectric Properties of Hot-Pressed Al- and Co-Doped Iron Disilicide Materials. *J. Alloys Compd.* **2007**, *438*, 303−309.

(42) Kresse, G.; Hafner, J. Ab Initio Molecular Dynamics for Liquid Metals. *Phys. Rev. B: Condens. Matter Mater. Phys.* **1993**, *47*, 558−561.

(43) Kresse, G.; Furthmüller, J. Efficient Iterative Schemes for Ab Initio Total-Energy Calculations Using a Plane-Wave Basis Set. *Phys. Rev. B: Condens. Matter Mater. Phys.* **1996**, *54*, 11169−11186.

(44) Kresse, G.; Joubert, D. From Ultrasoft Pseudopotentials to the Projector Augmented-Wave Method. *Phys. Rev. B: Condens. Matter Mater. Phys.* **1999**, *59*, 1758−1775.

(45) Sun, J. W.; Ruzsinszky, A.; Perdew, J. P. Strongly Constrained and Appropriately Normed Semilocal Density Functional. *Phys. Rev. Lett.* **2015**, *115*, 036402.

(46) Kirkpatrick, S.; Gelatt, C. D.; Vecchi, M. P. Optimization by Simulated Annealing. *Science* **1983**, *220*, 671−680.

(47) Zhang, S. B.; Northrup, J. E. Chemical Potential Dependence of Defect Formation Energies in GaAs: Application to Ga Self-Diffusion. *Phys. Rev. Lett.* **1991**, *67*, 2339−2342.

(48) Van de Walle, C. G.; Neugebauer, J. First-Principles Calculations for Defects and Impurities: Applications to III-Nitrides. *J. Appl. Phys.* **2004**, *95*, 3851−3879.

(49) Birkholz, U.; Schelm, J. Mechanism of Electrical Conduction in β-FeSi$_2$. *Phys. Status Solidi B* **1968**, *27*, 413−425.

(50) Chen, H. Y.; Zhao, X. B.; Zhu, T. J.; Lu, Y. F.; Ni, H. L.; Müller, E.; Mrotzek, A. Influence of Nitrogenizing and Al-Doping on Microstructures and Thermoelectric Properties of Iron Disilicide Materials. *Intermetallics* **2005**, *13*, 704−709.

(51) Rajasekar, P.; Umarji, A. M. Effect of Al-doping on Suppression of Thermal Conductivity in Si Dispersed β-FeSi$_2$. *Intermetallics* **2017**, *89*, 57−64.

(52) Kittel, C.; McEuen, P.; McEuen, P. *Introduction to Solid State Physics*; John Wiley & Sons: New York, 1956.

(53) May, A. F.; Toberer, E. S.; Saramat, A.; Snyder, G. J. Characterization and Analysis of Thermoelectric Transport in n-Type $Ba_8Ga_{16-x}Ge_{30+x}$. *Phys. Rev. B: Condens. Matter Mater. Phys.* **2009**, *80*, 125205.

(54) Kim, H. S.; Gibbs, Z. M.; Tang, Y. L.; Wang, H.; Snyder, G. J. Characterization of Lorenz Number with Seebeck Coefficient Measurement. *APL Mater.* **2015**, *3*, 041506.

(55) Umemoto, M. Preparation of Thermoelectric β-FeSi$_2$ Doped with Al and Mn by Mechanical Alloying (Overview). *Mater. Trans., JIM* **1995**, *36*, 373−383.

(56) Ito, M.; Nagai, H.; Oda, E.; Katsuyama, S.; Majima, K. Effects of P Doping on the Thermoelectric Properties of β-FeSi$_2$. *J. Appl. Phys.* **2002**, *91*, 2138.